In-Situ Construction of Fluorinated Solid-Electrolyte Interphase for Highly Reversible Zinc Anodes

Qinping Jian [a,1], Tianshuai Wang [a,1], Jing Sun [a], Maochun Wu [c,*], Tianshou Zhao [a,b,**]

[a] *Department of Mechanical and Aerospace Engineering, The Hong Kong University of Science and Technology, Clear Water Bay, Kowloon, Hong Kong SAR, 999077, China*

[b] *Department of Mechanical and Energy Engineering, Southern University of Science and Technology, Shenzhen, 518055, China*

[c] *Department of Mechanical Engineering, The Hong Kong Polytechnic University, Hung Hom, Kowloon, Hong Kong SAR, 999077, China*

[1] These authors contributed equally to this work.

[*] Corresponding author. E-mail: maochun.wu@polyu.edu.hk (M.C. Wu).

[**] Corresponding author. E-mail: zhaots@sustech.edu.cn (T.S. Zhao).

Acknowledgement

The work described in this paper was supported by the grants from the Research Grants Council of the Hong Kong Special Administrative Region, China (Project Nos. C5031-20G and 16205721) and Guangdong Basic and Applied Basic Research Foundation (Project No. 2021A1515011815)

CRediT author contribution statement

Qinping Jian: Conceptualization, Methodology, Investigation, Formal analysis, Writing original draft, Writing review & editing. **Tianshuai Wang**: Conceptualization, Methodology, Investigation, Writing review & editing. **Jing Sun**: Methodology, Writing review & editing. **Maochun Wu**: Methodology, Investigation, Writing review & editing, Supervision. **T.S. Zhao:** Conceptualization, Resources, Writing review & editing, Supervision, Project administration.

In-Situ Construction of Fluorinated Solid-Electrolyte Interphase for Highly Reversible Zinc Anodes

Abstract

Safe and low-cost aqueous zinc batteries offer a promise for energy storage. However, dendrite formation and parasitic reactions of zinc anodes hinder the practical application of this type of battery. In this work, guided by theoretical modeling, we formulate a new low-concentration electrolyte to boost the reversibility and stability of zinc anodes. Molecular dynamics simulations and first principle calculations reveal that adding dimethyl sulfoxide (DMSO) into a $Zn(TFSI)_2$ electrolyte can effectively introduce $TFSI^-$ anions into the solvation sheath of Zn^{2+}, of which the $TFSI^-$ anions will be preferably reduced prior to zinc deposition, thus in-situ forming a ZnF_2-rich interphase on the zinc surface. It is experimentally verified that the fluorinated interphase regulates the uniform zinc plating and stripping, thus suppressing the dendrite formation, and effectively prevents the zinc anode from side reactions with the electrolyte. As a result, the newly formulated electrolyte leads to highly reversible zinc plating/stripping with an average coulombic efficiency of as high as 98.4% and enables a zinc symmetric cell to achieve a long cycle life of over 2,000 h. More impressively, when the DMSO-modulated electrolyte is applied to full cells, a zinc-polyaniline battery can retain 87.9% of its initial capacity after 2,500 cycles at 2 A g^{-1}, and a zinc-activated carbon hybrid supercapacitor can stably cycle up to 20,000 times at 5 A g^{-1}. This work opens a new avenue for creating desirable solid-electrolyte interphase on the

zinc anode via facile electrolyte modulation, paving the way for development of high-performance aqueous zinc batteries.

Keywords: Zinc anode; Solid-electrolyte interphase; Electrolyte modulation; Solvation structure; Rechargeable aqueous battery

1. Introduction

Widespread adoption of renewable energies (e.g., solar and wind power) requires safe, efficient, and cost-effective grid-scale energy storage technologies to smooth out their intermittency and fluctuation [1–3]. Rechargeable aqueous zinc (Zn) batteries (RAZBs) hold tremendous potential for this application as Zn metal anode owns unique features, including high specific/volumetric capacity (820 mAh g^{-1} and 5855 mAh cm^{-3}), suitable redox potential (-0.76 V vs. standard hydrogen electrode), earth abundance, environmental friendliness, and low cost [4–9]. Moreover, when coupled with the non-flammable and highly ion-conductive aqueous electrolytes, RAZBs display outstanding rate performance and high safety compared with other counterparts [10,11]. Nevertheless, technological challenges arising from Zn dendrite growth, hazardous side reactions (e.g., hydrogen evolution reaction), and unstable Zn/electrolyte interface remain great obstacles for further development of RAZBs [12,13].

Thus far, various up-and-coming strategies have been proposed to address these challenges confronted by Zn anodes, such as electrode structure designs [14–16], electrode surface modifications [17–22], and electrolyte engineering [23–28]. Since the electrode-electrolyte interface plays a determining role in the electrochemical process, constructing a protective solid-electrolyte interphase (SEI) on the Zn surface is regarded as one of the most promising approaches to improving the performance of Zn anodes [29–31]. In general, an efficient SEI should allow facile, uniform Zn^{2+} transport while blocking the water penetration to the Zn surface. Meanwhile, high mechanical strength

is favored to further suppress dendrite growth. Of reported SEIs, zinc fluoride (ZnF_2) has attracted considerable attention owing to its intrinsic attractive properties, i.e., high Zn^{2+} ionic conductivity, electronic insulativity, and high mechanical strength [32–35]. For instance, ex-situ coating ZnF_2-based modification layer on the Zn surface using electrodeposition and vacuum pyrolysis has been demonstrated effectively in suppressing dendrite and side reactions of Zn anodes [32,35]. However, in addition to the high cost and complicated experimental procedures, the ex-situ coatings usually result in large thicknesses which may sacrifice the energy/power density and possess limited adaptability during the cycling.

On the contrary, in-situ construction of a ZnF_2-based SEI through electrolyte modulation is more facile and therefore more attractive. For instance, in a water-in-salt (WIS) electrolyte composed of 1 m $Zn(TFSI)_2$+20 m LiTFSI (m: mol kg^{-1}), a Zn^{2+} ion-conductive and water-blocking fluorinated SEI layer was in-situ formed on the Zn surface due to the decomposition of coordinated $TFSI^-$ anions upon cycling, thereby enabling a stable and highly reversible aqueous Zn anode[36]. Cao et al. designed a 4 m $Zn(OTf)_2$ electrolyte modified with trimethylethyl ammonium salt, and the synergistic reactions between OTf^- anion and trimethylethyl ammonium cation resulted in the generation of ZnF_2-based SEI on Zn anode [34]. Unfortunately, the intrinsic disadvantages (e.g., high salt cost and reduced ionic conductivity) of highly concentrated electrolytes hinder their practical application. In this regard, in-situ formation of SEI in low-concentration electrolytes is highly desired. To this end, Chu

et al. added a small amount of KPF_6 into the electrolyte, which would decompose spontaneously in aqueous environment and react with Zn metal to form a ZnF_2-rich SEI [37]. However, the SEI forming process is uncontrollable due to the spontaneous KPF_6 hydrolysis in an aqueous solution and would last until all KPF_6 is consumed. Therefore, it remains a challenge to in-situ construct a robust SEI in a non-concentrated aqueous electrolyte to boost the Zn electrochemistry.

Herein, guided by the theoretical modeling, a ZnF_2 SEI is in-situ formed on the Zn surface by formulating a new non-concentrated aqueous $Zn(TFSI)_2$ electrolyte (1 M) with dimethyl sulfoxide (DMSO) as the Zn^{2+} solvation regulator, which exhibits good chemical stability, high donor number (29.8), and low cost [38,39]. Molecular dynamics (MD) simulations reveal that adding a small amount of DMSO into $Zn(TFSI)_2$ electrolyte can significantly increase the portion of $TFSI^-$ anions in the primary solvation sheath of Zn^{2+}, while density functional theory (DFT) calculations indicate that the solvated $TFSI^-$ anions will be preferably reduced before Zn deposition, leading to the in-situ formation of fluorinated SEI layer on Zn surface. The solvation regulation strategy in the low-concentration electrolyte endows excellent advantages over highly concentrated electrolytes in terms of cost and ionic conductivity, and maintains good self-adaptivity in long-term cycling compared with the decomposing additives which undergo unstable reactions. Experimental results confirm that this functional fluorinated SEI can effectively suppress water-induced parasitic reactions and uniformize Zn^{2+} ion flux on the Zn anode, thus resulting in highly efficient Zn

plating/stripping and dendrite-free Zn deposition. It is demonstrated that the Zn anode in the DMSO-modified electrolyte can sustain long-term cycling over 2000 h in the symmetric cell without dendrite-induced short circuits. Furthermore, the DMSO-modulated electrolyte enables stable operation of full cells paired with diverse cathode materials, including polyaniline (PANI) and activated carbon (AC). This work not only provides a facile and efficient electrolyte regulation strategy to in situ construct robust ZnF_2-rich SEI, but also offers fresh insights into electrolyte formulation for highly reversible aqueous Zn anodes.

2. Results and discussion

Solvation structures of Zn^{2+} ions play a crucial role in the electrochemical behavior of Zn anode [40]. Hence, MD simulations were first performed to analyze the Zn^{2+} solvation structures in pure $Zn(TFSI)_2$ and $Zn(TFSI)_2$-DMSO aqueous systems (Figure 1a-c). In the pure $Zn(TFSI)_2$ system, radial distribution functions (RDFs) show that the primary solvation shell of Zn^{2+} is around 0.2 nm, which is composed of the Zn^{2+}-H_2O pair and Zn^{2+}-$TFSI^-$ pair. After the entire system was stabilized in the pure $Zn(TFSI)_2$ system, coordination number distribution functions (CNDs) reveal that there are 5.9 H_2O molecules and 0.1 $TFSI^-$ anion in the primary solvation shell (PSS) of Zn^{2+}. When DMSO additive is introduced, a new peak of Zn-O originating from DMSO appears at around 0.2 nm, indicating the participation of DMSO in the Zn^{2+} solvation structure. Then we further investigated the effect of DMSO content (volume ratio ranging from 15% to 70%, Figure S1) on the solvation structure. Note that the percentage of DMSO

thereafter is based on volume. It is found that the coordination number of the $TFSI^-$ anion in the solvation sheath changes with the increase of the DMSO content, reaching a maximum value of 0.6 when 30% DMSO is added. Considering the demand for increasing the ratio of $TFSI^-$ in PSS, the 30%-DMSO system is employed for the following investigations. To further analyze the effect of DMSO on the solvation structure, we calculated the number of hydrogen bonds in the 30% DMSO modified system and pristine $Zn(TFSI)_2$ electrolyte. Figure S2 shows that the number of hydrogen bonds in the $Zn(TFSI)_2$-DMSO electrolyte is smaller than that in the pure $Zn(TFSI)_2$ system, reflecting that the DMSO is helpful to destroy the original hydrogen-bond network inside the pure $Zn(TFSI)_2$ environment since they can push some H_2O out of the PSS. Therefore, the introduction of the 30% DMSO into the aqueous $Zn(TFSI)_2$ electrolyte can lead to a significant change in the Zn^{2+} solvation environment from a typical $Zn^{2+}[H_2O]_{5.9}[TFSI]_{0.1}$ to $Zn^{2+}[H_2O]_{5.1}[TFSI]_{0.6}[DMSO]_{0.3}$, indicating that DMSO can not only decrease the ratio of water but also increase the ratio of $TFSI^-$ anions in the Zn^{2+} solvation sheath.

To analyze the stability of the free and solvated species, quantum chemistry calculations were performed by adopting a cation-solvent/anion complex model. As shown in Figure 1d, the energy levels of the lowest unoccupied molecular orbital (LUMO) of the free DMSO and $TFSI^-$ anion are 0.75 and 0.32 eV, respectively. When Zn^{2+} is coordinated with DMSO and $TFSI^-$, their LUMO energy levels are significantly decreased to -2.75 and -2.81 eV, respectively. The lower LUMO levels of cation-solvent

or cation-anion complexes indicate that they are easier to receive electrons from the anode than free solvent/anions. The predicted reduction potentials (Figure 1e) of the free DMSO solvent (-1.92 V), free $TFSI^-$ anion (-2.44 V) and Zn^{2+}-DMSO complex (-0.06 V) are lower than that of the Zn^{2+}/Zn redox couple. Thus, the reductive decomposition of free DMSO, free $TFSI^-$ and Zn^{2+}-DMSO can hardly occur before Zn deposition, making it unable to form a protective SEI layer. In contrast, the Zn^{2+}-$TFSI^-$ complex becomes reductively unstable with a reduction potential of +0.16 V (*vs.* Zn^{2+}/Zn), which is further supported by the Mulliken charge analysis (Figure S3). It is well known that the electrons could preferably transfer from the cation to the anion unit and thus induce anion decomposition, based on the earlier reports that $TFSI^-$ can be reduced and react with Zn metal [33,36]. Therefore, it can be anticipated that this reduction process generates a ZnF_2 SEI on the Zn surface.

ZnF_2 is a semiconductor with a direct band gap of 3.44 eV as calculated in Figure S4. The ability for electron transfers from Zn to SEI was directly calculated from the density of states (DOS) profiles by taking the difference between the conduction band minimum and Fermi level (0 eV). As can be seen from Figure S5, the electron tunneling barrier between the Zn metal to ZnF_2 dramatically increases from 0 eV (layer 1) to over 1.5 eV at layer 4, proving that ZnF_2 is especially effective in blocking electron transfers from the Zn metal anode to the ZnF_2-rich SEI layer. In addition, it is calculated that ZnF_2 possesses a mechanical modulus of as high as 100 GPa, exceeding that of the Zn bulk phase (75 Gpa), which can effectively suppress the growth of Zn dendrite. Note

that the growth of Zn dendrite mainly occurs at the interface between Zn anode and the electrolyte in the initial cycling before the formation of the SEI layer. In this regard, the interactive behavior between Zn crystals and molecules in the electrolyte containing DMSO additives was investigated. Figure 1f compares the absorption energy (E_{abs}) of DMSO and water on the Zn slab. It is found that the interaction between Zn slab and H_2O is quite weak with an absorption energy of -0.25 eV, while DMSO interacts with Zn slab in a much stronger manner (E_{abs} = -0.63 eV) due to the short bond length of Zn-O. The charge density difference (Figure 1g and h) also reveals that there are more electrons transferred between the DMSO and Zn^{2+} than that of the H_2O system. These results indicate that DMSO is prone to be absorbed on the Zn surface in parallel, inhibiting the uncontrollable two-dimensional diffusion process and promoting more uniform Zn nucleation and deposition during the initial cycles.

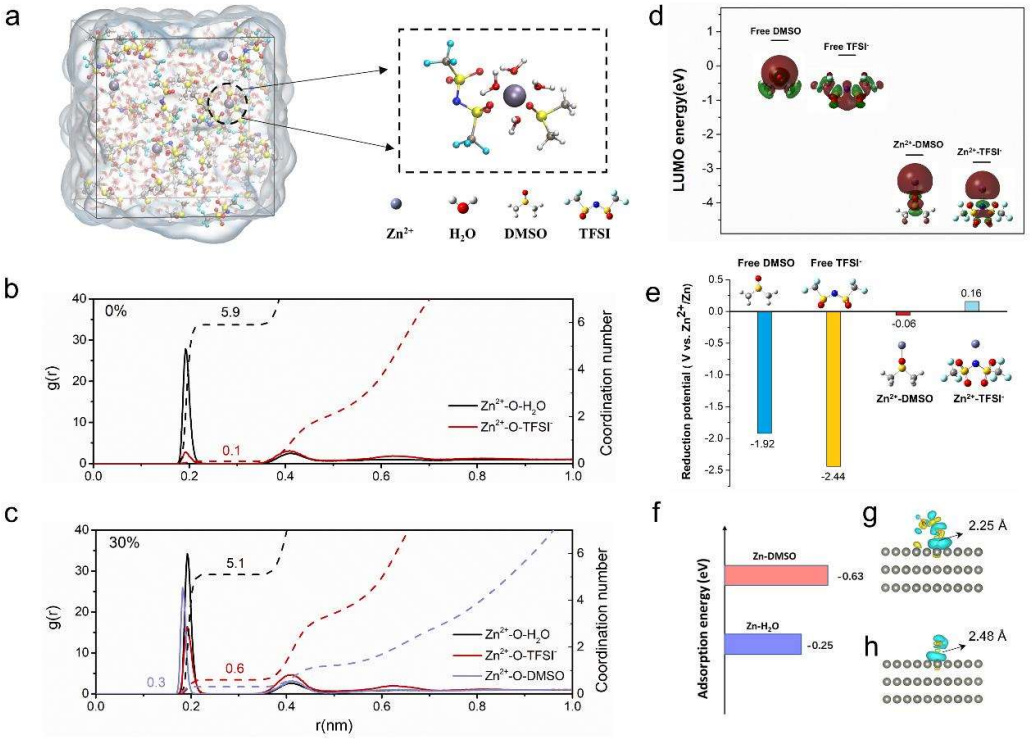

Figure 1. (a) The MD snapshot of 1 M $Zn(TFSI)_2$ with 30% DMSO. RDFs and CNDs of Zn^{2+}-groups pairs in (b) 1 M $Zn(TFSI)_2$ and (c) DMSO-modified 1 M $Zn(TFSI)_2$. (d) LUMO energy levels and (e) the predicted reduction potential with geometric structures of the free $TFSI^-$ anion, free DMSO solvent, and Zn^{2+}-$TFSI^-$ and Zn^{2+}–DMSO complexes. (f) Adsorption energies of DMSO and H_2O on Zn surface. (g) Charge density differences of DMSO and (h) H_2O adsorbed on Zn surface. The yellow section and blue section represent the charge accumulation and charge loss, respectively.

The interactions among various species and Zn^{2+} ions solvation structures in DMSO-modified electrolytes were then experimentally verified by various spectrum analyses. First, the interaction between DMSO and water molecules was probed using Fourier Transform Infrared Spectroscopy (FTIR). As displayed in Figure 2a, pure water exhibits a broad absorbance band located at 3000-3600 cm^{-1}, which is ascribed to the asymmetric O-H stretching in water molecules [41]. In the presence of the DMSO, the absorbance of the O-H band encountered an obvious red shift and a decreased peak intensity, indicating the original hydrogen bond network in water is weakened owing to the strong interaction between water and DMSO [42]. Figure 2b reveals that the S=O band of DMSO is shifted from 1042 cm^{-1} in pure DMSO to 1010 cm^{-1} in the 30% DMSO aqueous solution, which further proves the strong interaction between DMSO and water molecules. With the addition of the $Zn(TFSI)_2$, the S=O band at 1010 cm^{-1} moves to 1008 cm^{-1}, suggesting the existence of strong interaction between Zn^{2+} ions and DMSO. This is in line with the formation of metal-oxygen coordination between

Zn^{2+} ions and S=O groups of DMSO as calculated by MD simulations. The interaction between $TFSI^-$ anions and Zn^{2+} ions can be reflected by the FTIR bands of $-SO_3$ and $-CF_3$ groups in $TFSI^-$ anions which are proved to be sensitive to the cation–anion coordination [43–45]. As shown in Figure 2c, in the presence of DMSO, the $-CF_3$ group of $TFSI^-$ anion displays an obvious blue shift from 1197 to 1192 cm^{-1} and the $-SO_3$ band also shifted from 1325 to 1320 cm^{-1}. These results demonstrate that the addition of DMSO strengthens the interaction between the Zn^{2+} and $TFSI^-$ anions, resulting in an increased fraction of solvated $TFSI^-$ anions with Zn^{2+} ions in the DMSO-modified electrolyte [46].

Furthermore, the deconvolution analysis of the Raman vibration mode of $TFSI^-$ (Figure 2d) at the characteristic region of 730-760 cm^{-1} unveils that the Raman band consists of three modes at 740, 744, and 748 cm^{-1}, arising from free anions (FA), loose ion pairs (LIP), and intimate ion pairs (IIP), respectively [44,47,48]. The calculated fractions of FA, LIP and IIP in different solutions are displayed in Figure 2e. In pristine $Zn(TFSI)_2$ electrolyte, the majority of $TFSI^-$ anions (43%) exist as the form of FA, while LIP and IIP only account for 37% and 20%, respectively, suggesting the dominant monomeric Zn species coordinated by water molecules. In contrast, cation-anion coordination prevails in $Zn(TFSI)_2$-DMSO system, as evidenced by the significantly increased IIP (28%) and LIP (49%) mode and corresponding substantially lowered free anion fraction (23%). Owing to the intermolecular interactions, the coordinated $TFSI^-$ anion in the solvation sheath is expected to preferentially accept electrons and generate

the protective ZnF_2-rich SEI on the Zn surface during the deposition as illustrated in Figure 2f, which is also predicted by our DFT calculations. To verify the proposed mechanism, linear sweep voltammetry (LSV) measurements were conducted at 5 mV s^{-1} employing Ti foil as the working electrode, and Zn foil as the reference and counter electrodes. As displayed in Figure S6, the cell with DMSO-modified electrolyte exhibits an extra discernible reduction peak at -0.05 V (vs. Zn^{2+}/Zn) prior to Zn^{2+} plating (around -0.08 V), which is ascribed to the reduction of the anions from the Zn^{2+}–$TFSI^-$ complex, consistent with our DFT simulation results.

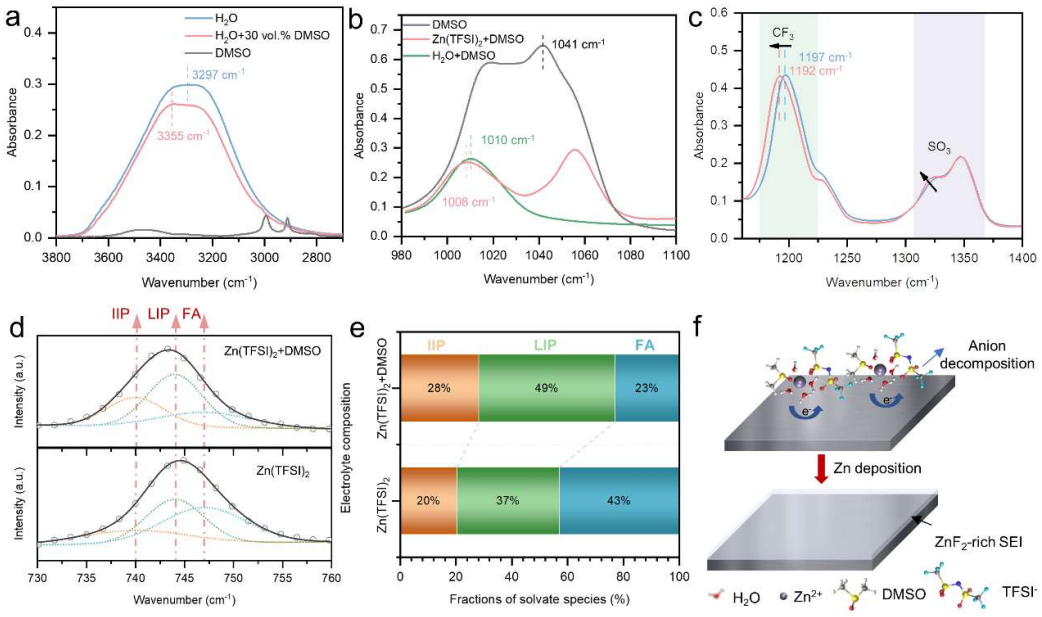

Figure 2. Analysis of interactions among different species in DMSO-modified $Zn(TFSI)_2$ electrolyte: FTIR spectra of (a) DMSO, water, and their mixture, (b) the S=O band of DMSO with and without $Zn(TFSI)_2$, and (c) the $-SO_3$ and $-CF_3$ band of $TFSI^-$ with and without DMSO. (d) Fitted Raman spectra of $Zn(TFSI)_2$ electrolyte with and without DMSO. Solid and dashed lines denote experimental spectra and fitting curves, respectively. (e) Solvate species distribution in electrolytes (free anions, loose ion pairs

and intimate ion pairs), obtained from the fitted Raman spectra. (f) Schematic illustration of the formation of the anion-derived ZnF_2-rich SEI on Zn surface.

The electrochemical performance of Zn anode in the newly designed electrolyte was first investigated by Cycling Voltammetry (CV). From Figure 3a, it can be seen that the ratio of reduction to oxidation current density in DMSO-modified electrolyte is higher than that of its pristine counterpart, indicating that the reversibility of the Zn plating and stripping is significantly enhanced in the presence of DMSO. The smaller reduction current density in DMSO-modified electrolyte possibly originates from the inhibited side reactions and the decreased ion diffusion coefficient as calculated from MD simulations (Figure S7). Moreover, the redox potentials for both Zn deposition and HER are negatively shifted, which may be attributed to the preferential adsorption of DMSO on the anode surface and SEI formation from the reduction of Zn^{2+}-$TFSI^-$ coordination[34]. Then chronoamperometry (CA) of Zn deposition at a constant overpotential (-150 mV) is conducted in different electrolytes. Note that the current density evolution in CA is an indicator reflecting the change in the actual surface area of the electrode [27,49]. As shown in Figure 3b, the current density of the Zn deposition in the pristine electrolyte shows a monotonous increase trend during the whole period of deposition (300 s), suggesting that the Zn^{2+} ions experience a rampant lateral diffusion aggregating at the nuclei and form dendrites which facilitates the fast growth of the electrode surface area. In sharp contrast, the current density of Zn deposition in the DMSO-modified electrolyte maintains a relatively constant value after the initial

2D diffusion process (Figure 3c), manifesting that the deposited Zn in the electrolyte with DMSO is relatively compact and uniform with minor increase in the surface area, which confirms that the absorbed DMSO and formed SEI constrain the lateral diffusion of Zn^{2+} ions.

Furthermore, the activation energy was measured to evaluate the energy barrier of the Zn deposition in different electrolytes. Based on the Nyquist plots of Zn/Zn symmetric cells under different temperatures from 308 to 328 K (Figure 3d and e) and the corresponding fitting resistance results, the relationship between charge transfer resistance (R_{ct}) and the temperature is plotted in Figure 3f, which is in accordance with the Arrhenius equation. Calculated results show that the activation energy (E_a) of Zn^{2+} deposition is reduced by 29% (from 59.4 to 42.2 kJ mol^{-1}) in the presence of DMSO. Because the main barrier of Zn^{2+} deposition originates from the Zn^{2+} de-solvation process [50,51], the reduced activation energy indicates that the de-solvation process is facilitated with the addition of DMSO. Figure S8 shows the contact angles of different electrolytes on Zn surface. The aqueous $Zn(TFSI)_2$ electrolyte displays a contact angle of 81°, whereas it is lowered to 65° with the addition of DMSO, which indicates weakened surface energy of DMSO-modified electrolyte [52]. The improved wettability of the electrolyte is conducive to the uniform distribution of Zn^{2+} ions on the Zn surface, which is essential for uniform Zn deposition [53]. Additionally, the DMSO-modified electrolyte exhibits a higher Zn^{2+} transference number (0.47) than that of the pristine $Zn(TFSI)_2$ electrolyte (0.19) (Figure S9). A higher transference number

means enhanced migration of the cations, which compensates for the decreased ion diffusivity of Zn^{2+} ions, inhibits anions diffusion and reduces the concentration polarizations, which is also conducive to the uniform Zn deposition [54]. LSV measurements in 0.1 M H_2SO_4 with and without DMSO were conducted to investigate the effects of DMSO on HER. As shown in Figure S10a, the HER onset potential (current density of HER reaches 1 mA cm^{-2}) in the bare 0.1 M H_2SO_4 is about -0.53 V, while it is retarded to -0.63 V with the addition of DMSO. In addition, the current density of the HER is significantly reduced in the presence of DMSO. These results demonstrate that adding DMSO in the electrolyte can effectively suppress the HER side reactions, thereby enhancing the stability of Zn electrodes. Furthermore, linear polarization measurements were employed to evaluate the anti-corrosion performance of Zn metal anode in different electrolytes. As displayed in Figure S10b, with the addition of DMSO, the corrosion current density is reduced and the corrosion potential positively shifts, indicating the improved corrosion resistance of Zn surface towards the side reactions, which is attributed to the protective effect of DMSO and the in-situ formation of SEI.

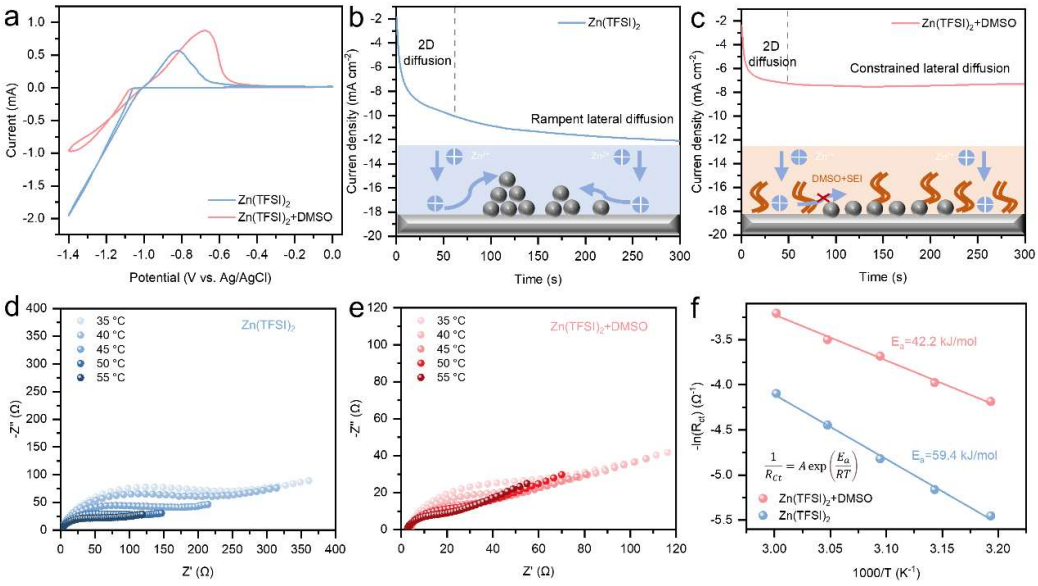

Figure 3. (a) CV curves of Zn plating/stripping at a scan rate of 5 mV s^{-1} (the fifth cycle). The CA curves measured at an overpotential of -150 mV in symmetric cells with: (b) pristine $Zn(TFSI)_2$ electrolyte and (c) DMSO-modified electrolyte. Nyquist plots at different temperatures of the Zn symmetric cells with: (d) pristine $Zn(TFSI)_2$ electrolyte and (e) DMSO-modified electrolyte. (f) Arrhenius curves and comparison of activation energies of Zn^{2+} deposition in Zn/Zn symmetric cells with different electrolytes.

To directly visualize the effect of DMSO-modified electrolyte on Zn deposition, home-made transparent symmetric cells (Figure S11) were assembled to in situ monitor Zn plating behavior on Zn surface using an optical microscope incorporated with a digital camera. The Zn plating was conducted at a current density of 2 mA cm^{-2} for 2 h. For bare $Zn(TFSI)_2$ electrolyte (Figure 4a and Movie S1), sparse nuclei and protrusions are clearly observed at the edge of the electrode after 2 min plating, which rapidly evolved into porous Zn clusters and dendrites, evidencing the uneven nucleation and electrodeposition. In sharp contrast, Zn nucleated uniformly and deposited compactly

on the electrode without forming dendritic clusters in the DMSO-modified electrolyte (Figure 4b and Movie S2). The in-situ observation confirms that the DMSO-modified electrolyte effectively homogenizes nucleation and suppresses Zn dendrite growth on Zn electrode.

The superiority of DMSO-modified $Zn(TFSI)_2$ electrolyte for stabilizing Zn anode was further evaluated in asymmetric and symmetric cells. The reversibility of Zn plating/stripping was first assessed by measuring the coulombic efficiency (CE) in Zn/Ti asymmetric cells adopting the "ion reservoir half-cell" protocol. As shown in Figure 4c, the Zn/Ti cells with different electrolytes are first galvanically cycled to diminish other effects (e.g., alloy formation and different electrode surface roughness) at 1 mA cm^{-2} with an areal capacity of 1 mAh cm^{-2} and a charge cut-off voltage of 1 V. Then, 1 mAh cm^{-2} of Zn (Q_p) is subsequently electrodeposited onto the Ti foil as a Zn reservoir, followed by cycling at a fixed capacity of 0.2 mAh cm^{-2} (Q_c) at 1 mA cm^{-2}. After n cycles (n equals 10 in this work), all removable Zn (Q_s) on Ti foil is fully stripped to a cutoff voltage of 1 V. The average CE could be obtained by the equation $CE_{ave} = (nQ_c + Q_s)/(nQ_c + Q_p)$. Results reveal that the cell with DMSO-modified electrolyte displays an average CE of as high as 98.4%, much higher than that using bare $Zn(TFSI)_2$ electrolyte (90.4%), indicating that the irreversible capacity loss of the Zn plating/stripping stemming from side reactions is considerably suppressed in the new electrolyte. Afterwards, Zn/Zn symmetric cells assembled with different electrolytes were cycled at different current densities and areal capacities to further

examine the cycling stability of Zn anodes. As presented in Figure 4d, the cell equipped with the DMSO-modified electrolyte exhibits a lower voltage hysteresis (32 mV) than that with the bare $Zn(TFSI)_2$ electrolyte (41 mV) at 1 mA cm^{-2} for 1 mA h cm^{-2}, which is ascribed to the reduced de-solvation energy consumption with the functional SEI. Remarkably, the $Zn(TFSI)_2$-DMSO electrolyte enables the cell to sustain extremely stable voltage polarizations for over 2000 h without internal short circuits, while the cell with the pristine Zn electrode undergoes fluctuating polarizations and suffers from short circuits only after around 50 h. When the current density is increased to 10 mA cm^{-2} (Figure S12), the cell with the bare electrolyte becomes short-circuited after only about 20 h, owing to the severe dendrite growth under a large current density. By comparison, the addition of DMSO allows the cell to stably cycle for over 200 h (1000 cycles), indicating that the functional SEI effectively inhibits Zn dendrite growth and side reactions. More impressively, the cell incorporated with DMSO-modified electrolyte can still maintain stable operation over 300 h even under a harsher condition (a high areal capacity of 5 mAh cm^{-2} at 5 mA cm^{-2}), whereas its un-modified counterpart can only operate for less than 50 h (Figure 4e). As summarized in Table S1, the Zn anode in this study outperforms many previous works, confirming the contribution of this newly formulated electrolyte in addressing the critical challenges of Zn anodes. These results demonstrate that the addition of DMSO $Zn(TFSI)_2$ electrolyte can boost the reversibility and stability of the Zn anode.

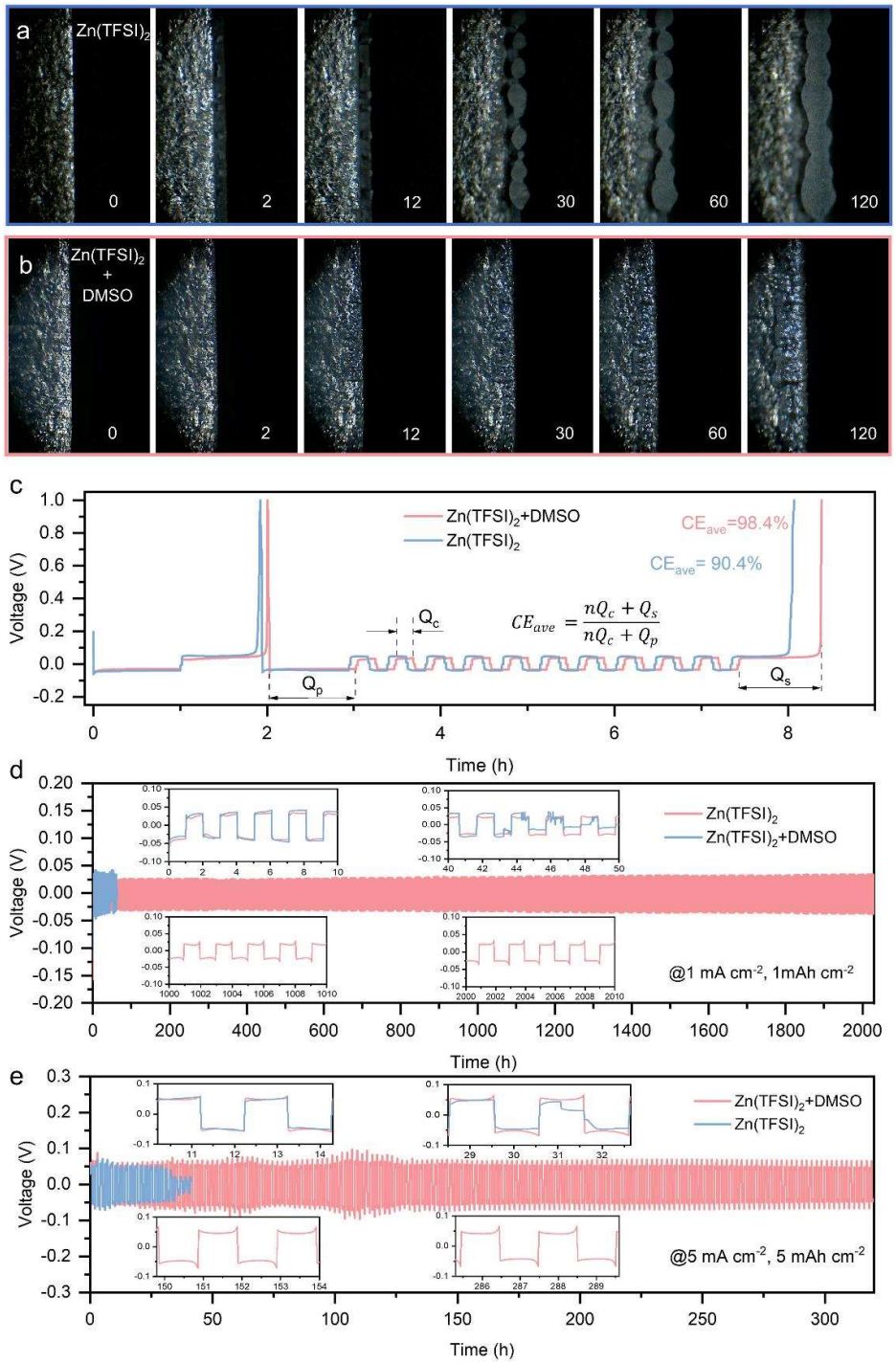

Figure 4. In situ optical microscopic observation of Zn plating/stripping processes in (a) base $Zn(TFSI)_2$ electrolyte and (b) DMSO-modified electrolyte on Zn electrode employing symmetric transparent cells at 2 mA cm^{-2}. (c) CE of Zn/Ti cells with bare $Zn(TFSI)_2$ electrolyte and DMSO-modified electrolyte. (d) Long-term galvanostatic

cycling of Zn/Zn symmetrical cells with bare $Zn(TFSI)_2$ electrolyte and DMSO-modified electrolyte at (d) 1 mA cm^{-2}, 1 mAh cm^{-2} and (e) 5 mA cm^{-2}, 5 mAh cm^{-2}.

Figure 5a and b display the morphologies of the cycled Zn anodes after 20 cycles at 1 mA cm^{-2}. It is clearly seen that the Zn surface cycled in the bare $Zn(TFSI)_2$ electrolyte becomes mossy and dendritic (Figure 5a1-a2), while a relatively smooth and compact surface without apparent dendrite formation is found on the Zn electrode cycled in DMSO-modified electrolyte (Figure 5b1-b2). As further evidenced by the cross-sectional Scanning Electron Microscopy (SEM) images, obvious dendrites are observed on the Zn surface in the absence of DMSO (Figure 5a3), which is inhibited effectively when DMSO is added (Figure 5b3). These results demonstrate the effectiveness of the newly formulated electrolyte in inhibiting Zn dendrite formation, which is attributable to the in-situ formed SEI. To verify this hypothesis, Raman spectra, Energy Dispersive Spectroscopy (EDS) mapping and X-ray photoelectron spectroscopy (XPS) were implemented to experimentally probe the existence of the in-situ formed SEI. The Raman spectra (Figure 5c) of the cycled Zn anode in DMSO-modified electrolyte shows a sharp characteristic peak of ZnF_2 located at 520 cm^{-1} [55], which is not observed in $Zn(TFSI)_2$ electrolyte, confirming that the cycled Zn surface is covered with a ZnF_2 containing SEI. This is further verified by SEM images and EDS mapping with uniform distribution of Zn and F elements as shown in Figure 5d. The surface composition of the SEI formed on Zn electrode after 20 cycles was further analyzed by XPS. As shown in Figure 5e, before sputtering, there is a distinct peak of $–CF_3$ species

(688.8 eV) from either the incomplete reduction of $TFSI^-$ or the trace salt on the Zn surface, while a small peak of inorganic ZnF_2 at 684.7 eV is observed in DMSO modified-electrolyte, resulting from the decomposition of anions of the Zn^{2+}-$TFSI^-$ coordination [45]. When the top layer of the interphase is removed using Ar^+ sputtering, the peak of ZnF_2 is clearly detected. In sharp contrast, no apparent ZnF_2 signal is detected on the cycled Zn anode in pristine $Zn(TFSI)_2$ electrolyte (Figure S13). It is also noted that the signals of sulfide (e.g., ZnS) apparently appear as the Ar^+ sputtering time increases (Figure S14a), further confirming the decomposition of the Zn^{2+}–$TFSI^-$ coordination and the involvement of decomposed species in the SEI formation. Similarly, no apparent signal of the ZnS is found on the Zn anode cycled in the pristine $Zn(TFSI)_2$ electrolyte (Figure S14b). Both theoretical and experimental results confirm that the addition of DMSO leads to the in-situ formation of a uniform ZnF_2-rich SEI, which could effectively homogenize Zn^{2+} ions distribution on the Zn surface and block the water molecules, thus inhibiting the Zn dendrite formation and hazardous water-induced side reactions.

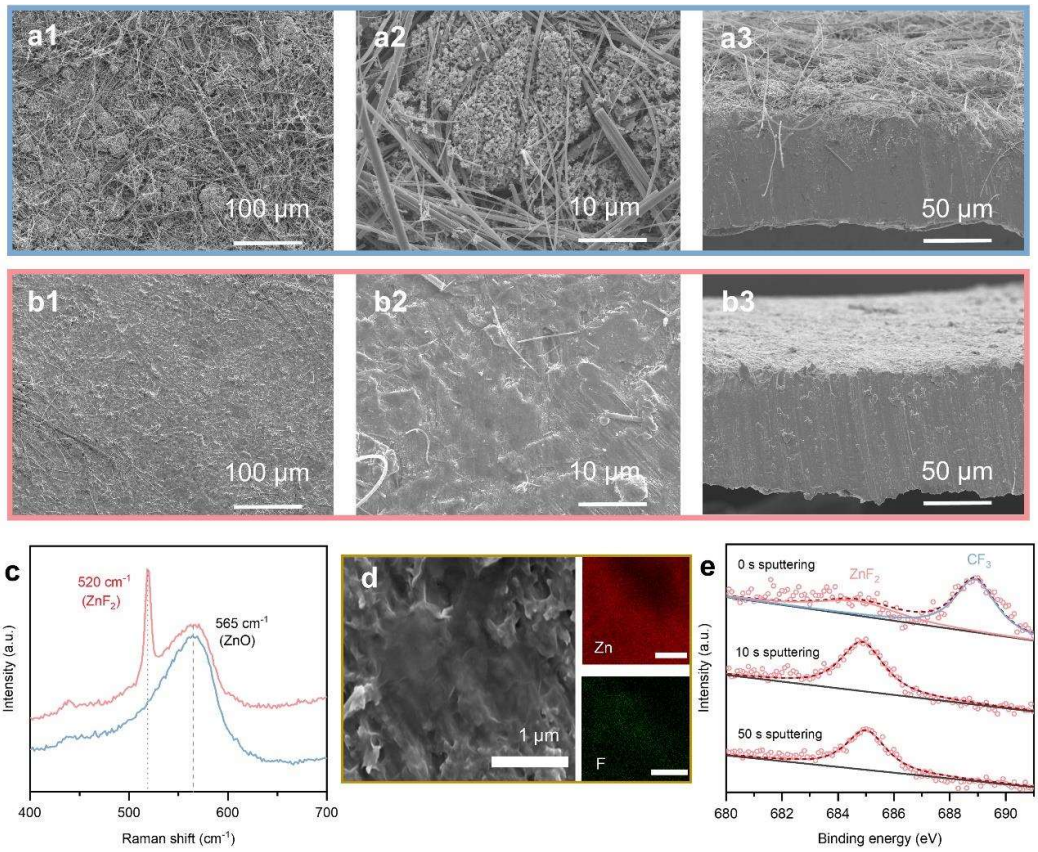

Figure 5. Morphologies of cycled Zn electrodes in (a1-a3) $Zn(TFSI)_2$ and (b1-b3) DMSO-modified electrolyte. SEI characterizations on the Zn electrode: (c) Raman spectra of the cycled Zn electrode in $Zn(TFSI)_2$ and DMSO modified electrolyte. (d) Element mapping results of Zn surface cycled in DMSO-modified electrolyte with Zn and F signal. (e) XPS spectral regions of F 1s for the cycled Zn electrode in DMSO-modified electrolyte as a function of corresponding Ar^+ sputtering time.

The practical application of the DMSO-modified electrolyte in aqueous Zn batteries is then evaluated in full cells composed of a Zn foil anode and different cathode materials, i.e, PANI and AC. The Zn/PANI full cells experience multi-step intercalation/deintercalation of Zn^{2+} and $TFSI^-$ (illustrated in Figure S15), respectively [56,57]. The CV curves of Zn-PANI full cells with different electrolytes are displayed

in Figure S16. There are two pairs of peaks which are ascribed to the intercalation/deintercalation of Zn^{2+} (Peak 1 and 2) and $TFSI^-$ (Peak 3 and 4), respectively. The peaks separation of the Peak 1 and 2 is narrowed with the presence of DMSO, suggesting that the reversibility of Zn^{2+} insertion/de-insertion into PANI is improved to some extent. The addition of DMSO shows minor effect on the $TFSI^-$ process, evidenced by the similar potentials and slight difference in different electrolytes, since the $TFSI^-$ anions in aqueous solution are hardly solvated by the water or other solvents [58,59]. Figure 6a shows the rate performance of the full Zn/PANI cells with various electrolytes. It is found that the cell with the DMSO-modified electrolyte delivers slightly higher discharge capacity than that with pristine $Zn(TFSI)_2$ electrolyte under low current densities (0.2-2 A g^{-1}), benefiting from the inhibited side reactions and dendrite formation. When the current density increases to 5 A g^{-1}, the discharge capacity becomes similar, which may result from the sacrificed ionic conductivity. With the current density returning to a small current (0.5 A g^{-1}), the cell with the DMSO-modified electrolyte maintains similar capacities with the initial cycles while the cell using pristine electrolyte delivers lower capacity than initial cycles, demonstrating the enhanced reversibility of the Zn anode in DMSO-modified electrolyte. The charge-discharge voltage profiles under various current densities are shown in Figure 6b. The cell with DMSO-modified electrolyte yields lower polarizations than the cell with pristine electrolyte owing to the improved electrochemical kinetics and suppressed side reactions. Figure 6c shows the long-term

cycling performance of the batteries with different electrolytes. After 2,500 cycles at 2 A g^{-1}, the Zn/PANI full cell with the DMSO-modified electrolyte still delivers a reversible discharge capacity of 108.4 mAh g^{-1}, corresponding to a high capacity retention of 87.9% or a capacity decay rate of as low as 0.005% per cycle, far surpassing that of the PANI/Zn battery assembled with pristine $Zn(TFSI)_2$ electrolyte, which retains only 60% of its initial capacity after 1500 cycles and suffers from internal short circuits after about 1850 cycles. The detailed charge/discharge curves at different cycles are displayed in Figure S17.

To further demonstrate the versatility of our electrolyte design for high-performance Zn metal anode, Zn-ion hybrid supercapacitors (ZHCs) were further constructed by using commercial AC as the cathode. The voltage profiles of the ZHCs with DMSO-modified electrolyte cycled under different current densities from 0.2 to 10 A g^{-1} are displayed in Figure S18. Even at a high rate of 10 A g^{-1}, the ZHC can still deliver a capacity of 63 mAh g^{-1}, demonstrating an excellent rate capability. Figure S19 shows the CV curves of AC at a scan rate of 5 mV s^{-1}. It can be seen that adding DMSO into the electrolyte displays minor effects on the electrochemical performance of AC cathode in terms of potential and shape of curves. This is because the $TFSI^-$ anions experience the adsorption/desorption processes during the charge and discharge process. Remarkably, the ZHC with the new electrolyte displays an ultralong cycling life of 20,000 cycles with a high capacity retention of 84.2% at 5 A g^{-1} (Figure 6d). By comparison, the ZHC with pristine electrolyte exhibits a poor capacity retention rate

and short-circuits after only about 2,000 cycles as shown in the inserted graph of voltage curves, indicating severe Zn dendrite growth during the cycles. The charge/discharge curves at different cycles are shown in Figure S20.The outstanding performance of Zn-PANI and ZHC full cells further proves the superior properties of DMSO-modified aqueous electrolytes, which induces a favorable solvation structure and in-situ formed robust SEI that boost the reversibility and stability of Zn anodes. Given the facile preparation, the low concentration, and excellent electrochemical properties, the newly proposed electrolyte holds great potential for practical applications.

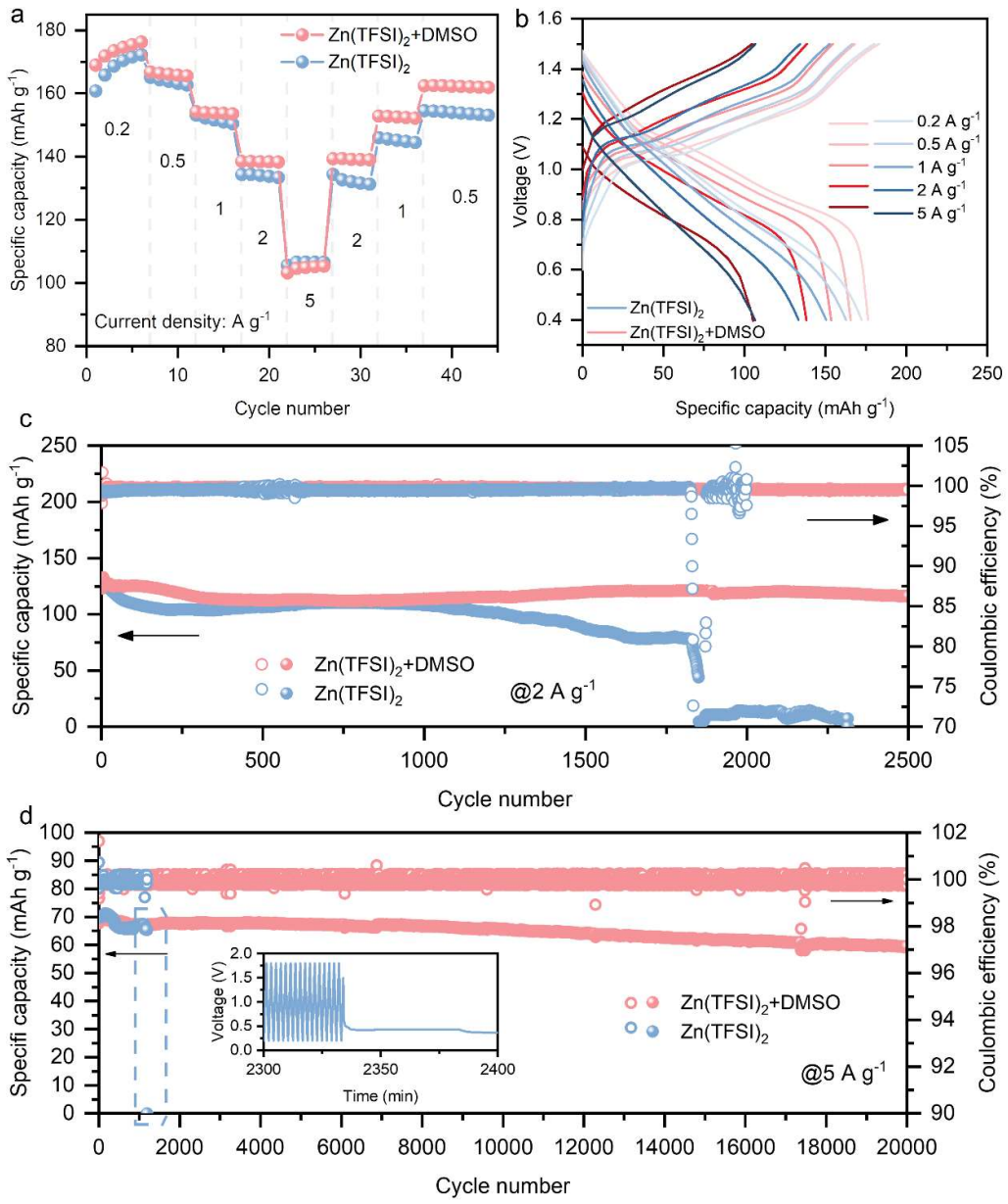

Figure 6. Electrochemical performance of Zn full cells. (a) Rate capability of Zn-PANI cells (b) Selected charge/discharge profiles of Zn-PANI cell with DMSO-modified electrolyte. Long-term cycling performance of the (c) Zn/PANI full cells at 2 A g^{-1} and (d) Zn/AC full cells at 5 A g^{-1}.

3. Conclusion

In summary, a DMSO-modulated, non-concentrated $Zn(TFSI)_2$ aqueous electrolyte is

successfully developed for highly stable and reversible Zn metal anodes. MD simulations and DFT calculations reveal that the addition of DMSO enables the formation of a Zn^{2+}-solvation sheath with the co-coordination of the DMSO solvent and $TFSI^-$ anion. This anion participated in the Zn^{2+} solvation sheath induces the preferential decomposition of $TFSI^-$ before Zn deposition, in-situ forming a ZnF_2-rich SEI layer on the Zn electrode, which regulates the uniform Zn plating/stripping and effectively suppresses the side reactions. As a result, the Zn symmetric cell is able to achieve an enhanced CE of 98.4% and maintain stable cycling over 2000 h. Furthermore, Zn full batteries that coupled with diverse cathode materials (e.g., PANI and AC) and the newly formulated electrolyte demonstrate remarkable cycling stability. This work offers a facile yet effective electrolyte modulation approach to address the critical challenges of Zn anodes, paving the way for the development of high-performance rechargeable aqueous batteries. The strategy may also inspire the design of efficient electrolytes for other rechargeable batteries.

4. Experimental section

4.1. Materials preparation

PANI nanorods (Figure S21) cathode material was prepared based on a given protocol with minor modification [56]. Briefly, 0.365 mL of aniline monomer was added into 15 mL of 1 M HCl acid solution under string in an ice bath. After string for 30 min, 0.228 g of ammonium persulfate was dissolved in 5 mL 1 M HCl acid solution and added into the prepared aniline solution dropwise under ice bath. The polymerization reaction

lasted for 1 h under vigorous stirring, and the samples were obtained and cleaned by centrifugation with deionized water and ethanol, and then dried at 60 °C overnight in an oven. The DMSO-modified electrolyte was prepared by adding various amounts of DMSO (99%, Sigma Aldrich) into the 1 M $Zn(TFSI)_2$ aqueous solution ($Zn(TFSI)_2$ salt, 99%, DodoChem). PANI and AC cathodes were prepared by blending 70 wt% PANI or AC (XFNANO Materials Tech Co., Ltd), 20 wt% Carbon Black and 10 wt% polyvinylidene fluoride (PVDF) and coating the slurry on carbon paper uniformly.

4.2. Materials characterizations

SEM (JSM-7100F (JEOL)) with EDS was used to observe the micro morphology of the Zn foils. XPS (AXIS Supra, Kratos) was used to determine the chemical states of the F1s element and S2p element of the Zn anodes. FTIR (Frontier NIR, PE) and Raman (InVia, Renishaw) spectra were used to obtain the characteristic absorbance curve of various electrolytes. Contact angles (Biolin Theta) were conducted to measure the wettability of the electrolytes on Zn foil using droplets (4 μL) of electrolytes as an indicator at room temperature.

4.3. Electrochemical measurements

Zn/Ti half cells, Zn/Zn symmetric cells and full cells (PANI-based AZBs and AC-based ZHCs) were assembled by using CR2025 coin-type cells and as-prepared electrolytes at room temperature. Electrodes were prepared by cutting Zn foils (thickness: 100 μm), Ti foils, PANI and AC cathodes with a diameter of 12 mm and, a piece of 18 mm glass fiber filter (Whatman) was used as a separator, respectively. The operating voltage

range of PANI-based AZBs and AC-based capacitors were 0.2-1.5 V and 0.2-1.8 V, respectively. Galvanostatic charge-discharge cycling was recorded by a battery testing system (Neware). CV test was conducted using a three-electrode configuration with glassy carbon as the working electrode, Pt mesh as the counter electrode and Ag/AgCl as the reference electrode. CV, EIS, CA and LSV were carried out on an electrochemical workstation (SP-200, Bio-logic). EIS tests were performed from 10^{-2} to 10^{5} Hz with an amplified voltage of 10 mV.

4.4 Theoretical calculations

Dynamic simulations were performed by the GROMACS 2018.8 simulation package with the AMBER99SB-ILDN force fields. Quantum chemistry calculations parts were performed using the Gaussian 09 package. All the ab-initial calculations were performed with the Vienna ab initio simulation package (VASP). Detailed simulation configurations are included in supporting information.

References

[1] H. Ibrahim, A. Ilinca, J. Perron, Energy storage systems-Characteristics and comparisons, Renew. Sustain. Energy. Rev. 12 (2008) 1221–1250.

[2] B. Dunn, H. Kamath, J.M. Tarascon, Electrical energy storage for the grid: A battery of choices, Science. 334 (2011) 928–935.

[3] J.B. Goodenough, Electrochemical energy storage in a sustainable modern society, Energy. Environ. Sci. 7 (2014) 14–18.

[4] C. Xu, B. Li, H. Du, F. Kang, Energetic zinc ion chemistry: The rechargeable zinc

ion battery, Angew. Chem. Int. Ed. 51 (2012) 933–935.

[5] T. Liu, X. Cheng, H. Yu, H. Zhu, N. Peng, R. Zheng, J. Zhang, M. Shui, Y. Cui, J. Shu, An overview and future perspectives of aqueous rechargeable polyvalent ion batteries, Energy Storage Mater. 18 (2019) 68–91.

[6] C. Li, X. Xie, S. Liang, J. Zhou, Issues and Future Perspective on Zinc Metal Anode for Rechargeable Aqueous Zinc- ion Batteries, Energy. Environ. Mater. 3 (2020) 146–159.

[7] A. Konarov, N. Voronina, J.H. Jo, Z. Bakenov, Y.-K. Sun, S.-T. Myung, Present and Future Perspective on Electrode Materials for Rechargeable Zinc-Ion Batteries, ACS Energy Lett. 3 (2018) 2620–2640.

[8] M. Jiao, Q. Zhang, C. Ye, Z. Liu, X. Zhong, J. Wang, C. Li, L. Dai, G. Zhou, H.M. Cheng, Recycling spent LiNi1-x-yMnxCoyO2 cathodes to bifunctional NiMnCo catalysts for zinc-air batteries, Proc. Natl. Acad. Sci. U. S. A. 119 (2022) e2202202119.

[9] Q. Huang, X. Zhong, Q. Zhang, X. Wu, M. Jiao, B. Chen, J. Sheng, G. Zhou, Co3O4/Mn3O4 hybrid catalysts with heterointerfaces as bifunctional catalysts for Zn-air batteries, J. Energy Chem. 68 (2022) 679–687.

[10] J. Wang, Y. Yang, Y. Zhang, Y. Li, R. Sun, Z. Wang, H. Wang, Strategies towards the challenges of zinc metal anode in rechargeable aqueous zinc ion batteries, Energy Storage Mater. 35 (2021) 19–46.

[11] S. Huang, J. Zhu, J. Tian, Z. Niu, Recent Progress in the Electrolytes of Aqueous Zinc-Ion Batteries, Chem. Eur. J. 25 (2019) 14480–14494.

[12] Z. Cao, P. Zhuang, X. Zhang, M. Ye, J. Shen, P.M. Ajayan, Z. Cao, P. Zhuang, M. Ye, J. Shen, X. Zhang, M. Ajayan, Strategies for Dendrite-Free Anode in Aqueous Rechargeable Zinc Ion Batteries, Adv. Energy Mater. 10 (2020) 2001599.

[13] H. Jia, Z. Wang, B. Tawiah, Y. Wang, C.Y. Chan, B. Fei, F. Pan, Recent advances in zinc anodes for high-performance aqueous Zn-ion batteries, Nano Energy. 70 (2020) 104523.

[14] Z. Wang, J. Huang, Z. Guo, X. Dong, Y. Liu, Y. Wang, Y. Xia, A Metal-Organic Framework Host for Highly Reversible Dendrite-free Zinc Metal Anodes, Joule. 3 (2019) 1289–1300.

[15] W. Guo, Z. Cong, Z. Guo, C. Chang, X. Liang, Y. Liu, W. Hu, X. Pu, Dendrite-free Zn anode with dual channel 3D porous frameworks for rechargeable Zn batteries, Energy Storage Mater. 30 (2020) 104–112.

[16] Q. Jian, Z. Guo, L. Zhang, M. Wu, T. Zhao, A hierarchical porous tin host for dendrite-free, highly reversible zinc anodes, Chem. Eng. J. 425 (2021) 130643.

[17] J. Zhou, M. Xie, F. Wu, Y. Mei, Y. Hao, R. Huang, G. Wei, A. Liu, L. Li, R. Chen, Ultrathin Surface Coating of Nitrogen-Doped Graphene Enables Stable Zinc Anodes for Aqueous Zinc-Ion Batteries, Adv. Mater. 33 (2021) 2101649.

[18] L. Kang, M. Cui, F. Jiang, Y. Gao, H. Luo, J. Liu, W. Liang, C. Zhi, Nanoporous CaCO3 Coatings Enabled Uniform Zn Stripping/Plating for Long-Life Zinc Rechargeable Aqueous Batteries, Adv. Energy Mater. 8 (2018) 1801090.

[19] X. Xie, S. Liang, J. Gao, S. Guo, J. Guo, C. Wang, G. Xu, X. Wu, G. Chen, J. Zhou,

Manipulating the ion-transfer kinetics and interface stability for high-performance zinc metal anodes, Energy. Environ. Sci. 13 (2020) 503–510.

[20] Q. Jian, Y. Wan, J. Sun, M. Wu, T. Zhao, A dendrite-free zinc anode for rechargeable aqueous batteries, J. Mater. Chem. A. 8 (2020) 20175–20184.

[21] H. He, H. Qin, J. Wu, X. Chen, R. Huang, F. Shen, Z. Wu, G. Chen, S. Yin, J. Liu, Engineering interfacial layers to enable Zn metal anodes for aqueous zinc-ion batteries, Energy Storage Mater. 43 (2021) 317–336.

[22] Z. Yang, Q. Zhang, C. Xie, Y. Li, W. Li, T. Wu, Y. Tang, H. Wang, Electrochemical interface reconstruction to eliminate surface heterogeneity for dendrite-free zinc anodes, Energy Storage Mater. 47 (2022) 319–326.

[23] Q.P. Jian, M.C. Wu, H.R. Jiang, Y.K. Lin, T.S. Zhao, A trifunctional electrolyte for high-performance zinc-iodine flow batteries, J. Power Sources. 484 (2021) 229238.

[24] Y. Jin, K.S. Han, Y. Shao, M.L. Sushko, J. Xiao, H. Pan, J. Liu, Y. Jin, Y. Shao, J. Xiao, H. Pan, J. Liu, K.S. Han, M.L. Sushko, Stabilizing Zinc Anode Reactions by Polyethylene Oxide Polymer in Mild Aqueous Electrolytes, Adv. Funct. Mater. 30 (2020) 2003932.

[25] W. Xu, K. Zhao, W. Huo, Y. Wang, G. Yao, X. Gu, H. Cheng, L. Mai, C. Hu, X. Wang, Diethyl ether as self-healing electrolyte additive enabled long-life rechargeable aqueous zinc ion batteries, Nano Energy. 62 (2019) 275–281.

[26] Q. Zhang, J. Luan, L. Fu, S. Wu, Y. Tang, X. Ji, H. Wang, The Three-Dimensional Dendrite-Free Zinc Anode on a Copper Mesh with a Zinc-Oriented Polyacrylamide

Electrolyte Additive, Angew. Chem. Int. Ed. 58 (2019) 15841–15847.

[27] A. Bayaguud, X. Luo, Y. Fu, C. Zhu, Cationic surfactant-type electrolyte additive enables three-dimensional dendrite-free zinc anode for stable zinc-ion batteries, ACS Energy Lett. 5 (2020) 3012–3020.

[28] Q. Zhang, Y. Ma, Y. Lu, X. Zhou, L. Lin, L. Li, Z. Yan, Q. Zhao, K. Zhang, J. Chen, Designing Anion- Type Water- Free Zn 2+ Solvation Structure for Robust Zn Metal Anode, Angew. Chem. Int. Ed. 133 (2021) 23545–23552.

[29] Q. Zhang, J. Luan, Y. Tang, X. Ji, H. Wang, Interfacial Design of Dendrite-Free Zinc Anodes for Aqueous Zinc-Ion Batteries, Angew. Chem. Int. Ed. 59 (2020) 13180–13191.

[30] F. Tao, Y. Liu, X. Ren, J. Wang, Y. Zhou, Y. Miao, F. Ren, S. Wei, J. Ma, Different surface modification methods and coating materials of zinc metal anode, J. Energy Chem. 66 (2022) 397–412.

[31] Q. Jian, Y. Wan, Y. Lin, M. Ni, M. Wu, T. Zhao, A highly reversible zinc anode for rechargeable aqueous batteries, ACS Appl. Mater. Interfaces. 13 (2021) 52659–52669.

[32] L. Ma, Q. Li, Y. Ying, F. Ma, S. Chen, Y. Li, H. Huang, C. Zhi, L.T. Ma, Q. Li, F.X. Ma, S. Chen, Y.Y. Li, C. Zhi, Y.R. Ying, H.T. Huang, Toward Practical High-Areal-Capacity Aqueous Zinc-Metal Batteries: Quantifying Hydrogen Evolution and a Solid-Ion Conductor for Stable Zinc Anodes, Adv. Mater. 33 (2021) 2007406.

[33] H. Qiu, X. Du, J. Zhao, Y. Wang, J. Ju, Z. Chen, Z. Hu, D. Yan, X. Zhou, G. Cui, Zinc anode-compatible in-situ solid electrolyte interphase via cation solvation

modulation, Nat. Commun. 10 (2019) 1–12.

[34] L. Cao, D. Li, T. Pollard, T. Deng, B. Zhang, C. Yang, L. Chen, J. Vatamanu, E. Hu, M.J. Hourwitz, L. Ma, M. Ding, Q. Li, S. Hou, K. Gaskell, J.T. Fourkas, X.-Q. Yang, K. Xu, O. Borodin, C. Wang, Fluorinated interphase enables reversible aqueous zinc battery chemistries, Nat. Nanotechnol. 16 (2021) 902–910.

[35] Y. Yang, C. Liu, Z. Lv, H. Yang, Y. Zhang, M. Ye, L. Chen, J. Zhao, C.C. Li, Synergistic Manipulation of Zn2+ Ion Flux and Desolvation Effect Enabled by Anodic Growth of a 3D ZnF2 Matrix for Long-Lifespan and Dendrite-Free Zn Metal Anodes, Adv. Mater. 33 (2021) 2007388.

[36] F. Wang, O. Borodin, T. Gao, X. Fan, W. Sun, F. Han, A. Faraone, J.A. Dura, K. Xu, C. Wang, Highly reversible zinc metal anode for aqueous batteries, Nat. Mater. 17 (2018) 543–549.

[37] Y. Chu, S. Zhang, S. Wu, Z. Hu, G. Cui, J. Luo, In situ built interphase with high interface energy and fast kinetics for high performance Zn metal anodes, Energy. Environ. Sci. 14 (2021) 3609–3620.

[38] M. Katayama, M. Shinoda, K. Ozutsumi, S. Funahashi, Y. Inada, Reevaluation of Donor Number Using Titration Calorimetry, Anal. Sci. 28 (2012) 103–103.

[39] C.O. Laoire, S. Mukerjee, K.M. Abraham, E.J. Plichta, M.A. Hendrickson, Influence of Nonaqueous Solvents on the Electrochemistry of Oxygen in the Rechargeable Lithium−Air Battery, J. Phys. Chem. C. 114 (2010) 9178–9186.

[40] Jin Cao, Dongdong Zhang, Xinyu Zhang, Zhiyuan Zeng, Jiaqian Qin,

Yunhui Huang, Strategies of regulating Zn 2+ solvation structures for dendrite-free and side reaction-suppressed zinc-ion batteries, Energy. Environ. Sci. 15 (2022) 499–528.

[41] B.L. Mojet, S.D. Ebbesen, L. Lefferts, Light at the interface: the potential of attenuated total reflection infrared spectroscopy for understanding heterogeneous catalysis in water, Chem. Soc. Rev. 39 (2010) 4643–4655.

[42] Y. Dong, L. Miao, G. Ma, S. Di, Y. Wang, L. Wang, J. Xu, N. Zhang, Non-concentrated aqueous electrolytes with organic solvent additives for stable zinc batteries, Chem. Sci. 12 (2021) 5843–5852.

[43] W.A. Henderson, Glyme-lithium salt phase behavior, J. Phys. Chem. B. 110 (2006) 13177–13183.

[44] D.M. Seo, O. Borodin, S.-D. Han, P.D. Boyle, W.A. Henderson, Electrolyte Solvation and Ionic Association II. Acetonitrile-Lithium Salt Mixtures: Highly Dissociated Salts, J. Electrochem. Soc. 159 (2012) A1489–A1500.

[45] H. Qiu, X. Du, J. Zhao, Y. Wang, J. Ju, Z. Chen, Z. Hu, D. Yan, X. Zhou, G. Cui, Zinc anode-compatible in-situ solid electrolyte interphase via cation solvation modulation, Nat. Commun. 10 (2019) 5374.

[46] Y. Hu, Z. Wang, H. Li, X. Huang, L. Chen, Spectroscopic studies on the cation–anion, cation–solvent and anion–solvent interactions in the LiCF3SO3/acetamide complex system, Spectrochim. Acta - A: Mol. Biomol. 61 (2005) 403–411.

[47] L. Suo, D. Oh, Y. Lin, Z. Zhuo, O. Borodin, T. Gao, F. Wang, A. Kushima, Z. Wang, H.C. Kim, Y. Qi, W. Yang, F. Pan, J. Li, K. Xu, C. Wang, How Solid-Electrolyte

Interphase Forms in Aqueous Electrolytes, J. Am. Chem. Soc. 139 (2017) 18670–18680.

[48] Y. Yamada, K. Furukawa, K. Sodeyama, K. Kikuchi, M. Yaegashi, Y. Tateyama, A. Yamada, Unusual stability of acetonitrile-based superconcentrated electrolytes for fast-charging lithium-ion batteries, J. Am. Chem. Soc. 136 (2014) 5039–5046.

[49] Z. Zhao, J. Zhao, Z. Hu, J. Li, J. Li, Y. Zhang, C. Wang, G. Cui, Long-life and deeply rechargeable aqueous Zn anodes enabled by a multifunctional brightener-inspired interphase, Energy. Environ. Sci. 12 (2019) 1938–1949.

[50] D. Kundu, S. Hosseini Vajargah, L. Wan, B. Adams, D. Prendergast, L.F. Nazar, Aqueous vs. nonaqueous Zn-ion batteries: consequences of the desolvation penalty at the interface, Energy. Environ. Sci. 11 (2018) 881–892.

[51] X. Xie, S. Liang, J. Gao, S. Guo, J. Guo, C. Wang, G. Xu, X. Wu, G. Chen, J. Zhou, Manipulating the ion-transfer kinetics and interface stability for high-performance zinc metal anodes, Energy. Environ. Sci. 13 (2020) 503–510.

[52] Z. Zhang, W. Wang, A.N. Korpacz, C.R. Dufour, Z.J. Weiland, C.R. Lambert, M.T. Timko, Binary Liquid Mixture Contact-Angle Measurements for Precise Estimation of Surface Free Energy, Langmuir. 35 (2019) 12317–12325.

[53] J. Hao, L. Yuan, C. Ye, D. Chao, K. Davey, Z. Guo, S.Z. Qiao, Boosting Zinc Electrode Reversibility in Aqueous Electrolytes by Using Low-Cost Antisolvents, Angew. Chem. Int. Ed. 60 (2021) 7366–7375.

[54] M. Zhu, J. Hu, Q. Lu, H. Dong, D.D. Karnaushenko, C. Becker, D. Karnaushenko, Y. Li, H. Tang, Z. Qu, J. Ge, O.G. Schmidt, M. Zhu, H. Dong, D.D. Karnaushenko, C.

Becker, D. Karnaushenko, Y. Li, H. Tang, Z. Qu, J. Ge, O.G. Schmidt, J. Hu, Q. Lu, A Patternable and In Situ Formed Polymeric Zinc Blanket for a Reversible Zinc Anode in a Skin-Mountable Microbattery, Adv. Mater. 33 (2021) 2007497.

[55] S.P.S. Porto, P.A. Fleury, T.C. Damen, Raman Spectra of TiO2, MgF2, ZnF2, FeF2, and MnF2, Phys. Rev. 154 (1967) 522–526.

[56] F. Wan, L. Zhang, X. Wang, S. Bi, Z. Niu, J. Chen, F. Wan, L. Zhang, X. Wang, S. Bi, Z. Niu, J. Chen, An Aqueous Rechargeable Zinc-Organic Battery with Hybrid Mechanism, Adv. Func. Mater. 28 (2018) 1804975.

[57] H.Y. Shi, Y.J. Ye, K. Liu, Y. Song, X. Sun, A Long-Cycle-Life Self-Doped Polyaniline Cathode for Rechargeable Aqueous Zinc Batteries, Angew. Chem. Int. Ed. 57 (2018) 16359–16363.

[58] T. Zhang, Y. Tang, S. Guo, X. Cao, A. Pan, G. Fang, J. Zhou, S. Liang, Fundamentals and perspectives in developing zinc-ion battery electrolytes: a comprehensive review, Energy Environ. Sci. 13 (2020) 4625–4665.

[59] Y. Wang, Z. Wang, F. Yang, S. Liu, S. Zhang, J. Mao, Z. Guo, Y. Wang, Z. Wang, F. Yang, S. Liu, S. Zhang, J. Mao, Z. Guo, Electrolyte Engineering Enables High Performance Zinc-Ion Batteries, Small. (2022) 2107033.